

# A dynamic mixed subgrid-scale model and its application to turbulent recirculating flows

Yan Zang, Robert L. Street, and Jeffrey R. Koseff

Citation: *Physics of Fluids A: Fluid Dynamics* **5**, 3186 (1993); doi: 10.1063/1.858675

View online: <https://doi.org/10.1063/1.858675>

View Table of Contents: <https://aip.scitation.org/toc/pfa/5/12>

Published by the *American Institute of Physics*

---

## ARTICLES YOU MAY BE INTERESTED IN

[A dynamic subgrid-scale eddy viscosity model](#)

*Physics of Fluids A: Fluid Dynamics* **3**, 1760 (1991); <https://doi.org/10.1063/1.857955>

[A proposed modification of the Germano subgrid-scale closure method](#)

*Physics of Fluids A: Fluid Dynamics* **4**, 633 (1992); <https://doi.org/10.1063/1.858280>

[A dynamic subgrid-scale model for compressible turbulence and scalar transport](#)

*Physics of Fluids A: Fluid Dynamics* **3**, 2746 (1991); <https://doi.org/10.1063/1.858164>

[On the formulation of the dynamic mixed subgrid-scale model](#)

*Physics of Fluids* **6**, 4057 (1994); <https://doi.org/10.1063/1.868333>

[An eddy-viscosity subgrid-scale model for turbulent shear flow: Algebraic theory and applications](#)

*Physics of Fluids* **16**, 3670 (2004); <https://doi.org/10.1063/1.1785131>

[Direct numerical simulation of turbulent channel flow up to  \$Re\_\tau=590\$](#)

*Physics of Fluids* **11**, 943 (1999); <https://doi.org/10.1063/1.869966>

---

# A dynamic mixed subgrid-scale model and its application to turbulent recirculating flows

Yan Zang, Robert L. Street, and Jeffrey R. Koseff

*Environmental Fluid Mechanics Laboratory, Stanford University, Stanford, California 94305-4020*

(Received 3 February 1993; accepted 27 July 1993)

The dynamic subgrid-scale eddy viscosity model of Germano *et al.* [Phys. Fluids A 3, 1760 (1991)] (DSM) is modified by employing the mixed model of Bardina *et al.* [Ph.D dissertation, Stanford University, 1983] as the base model. The new dynamic mixed model explicitly calculates the modified Leonard term and only models the cross term and the SGS Reynolds stress. It retains the favorable features of DSM and, at the same time, does not require that the principal axes of the stress tensor be aligned with those of the strain rate tensor. The model coefficient is computed using local flow variables. The new model is incorporated in a finite-volume solution method and large-eddy simulations of flows in a lid-driven cavity at Reynolds numbers of 3200, 7500, and 10 000 show excellent agreement with the experimental data. Better agreement is achieved by using the new model compared to the DSM. The magnitude of the dynamically computed model coefficient of the new model is significantly smaller than that from DSM.

## I. INTRODUCTION

Most engineering and environmental flows are turbulent and occur in geometrically complex domains. Direct numerical simulation (DNS) is restricted to low-Reynolds number turbulent flows due to the necessity of resolving all the spatial scales of the motion. On the other hand, large eddy simulation (LES) provides an effective tool for tackling complex turbulent flows by computing only the large-scale motions and modeling the subgrid scales.

The key to the success of large eddy simulation is to accurately represent the unresolved subgrid-scale (SGS) motions. For inhomogeneous, complex turbulent flows, it is necessary that the SGS model adjusts to local flow dynamics. The most widely used SGS model is the Smagorinsky model<sup>1</sup> in which the anisotropic part of the SGS stress is

$$\tau_{ij} - \frac{\delta_{ij}}{3} \tau_{kk} = -2\nu_T \bar{S}_{ij}, \quad (1)$$

where the eddy viscosity is

$$\nu_T = C\bar{\Delta}^2 |\bar{S}|, \quad (2)$$

$C$  is the dimensionless model coefficient,  $\bar{\Delta}$  is the grid-filter width, and  $|\bar{S}| = (2\bar{S}_{ij}\bar{S}_{ij})^{1/2}$  is the magnitude of the resolved strain rate tensor

$$\bar{S}_{ij} = \frac{1}{2} \left( \frac{\partial \bar{u}_i}{\partial x_j} + \frac{\partial \bar{u}_j}{\partial x_i} \right).$$

This model, though very popular, has some notable drawbacks which include that it (a) requires an input model coefficient  $C$  which is flow dependent; (b) predicts incorrect asymptotic behavior near a wall or in a laminar flow; (c) does not allow SGS energy backscatter to the resolved scales; and (d) assumes that the principal axes of the SGS stress tensor are aligned with those of the resolved strain rate tensor, a result which is not supported by direct numerical simulation data.<sup>2</sup> Furthermore, the Smagorin-

sky model is too dissipative in LES of wall-bounded transitional flows,<sup>3</sup> and correlates poorly with DNS data in both homogeneous turbulence<sup>2</sup> and turbulent channel flow.<sup>4</sup>

Extensive effort has been made to improve on the Smagorinsky model. Damping functions were used in order to account for the near-wall effect.<sup>5,6</sup> Yakhot and Orszag<sup>7</sup> and Yakhot *et al.*<sup>8</sup> developed a subgrid-scale model based on the Renormalization Group theory and applied it to the LES of turbulent channel flow. This model avoids the use of a damping function by taking into account the near-wall damping effect of the normal shear stress, but the asymptotic behavior that it predicts depends on the grid resolution. Horiuti<sup>9</sup> employed the SGS normal shear stress instead of the SGS total energy as the velocity scale in an eddy viscosity model and reported improved correlation with the DNS data in a turbulent channel flow. The eddy viscosity model that Horiuti proposed was shown to act similarly as the Van Driest damping function<sup>10</sup> in the near-wall region. This model is yet to be extended to turbulent flows in more complex geometries.

Recently, Germano *et al.*<sup>11</sup> developed a dynamic SGS model (DSM) which overcomes some of the aforementioned drawbacks of the Smagorinsky model. Utilizing an algebraic identity suggested by Germano,<sup>12</sup> DSM calculates the model coefficient using the information from the smallest resolved scales. This model has many desirable features in that it requires only one input parameter, exhibits the correct asymptotic behavior near a solid wall and in a laminar flow, and does not prohibit energy backscatter. DSM has been successfully applied to LES of transitional and turbulent channel flows<sup>11</sup> and both incompressible and compressible isotropic turbulence.<sup>13</sup> In these simulations, however, the dynamically computed model coefficient was averaged either in the global volume of the domain or in a homogeneous plane.

In spite of its remarkable success, DSM has several aspects that need improvement. Because the Smagorinsky

model is employed as the base model, DSM is an eddy viscosity model which requires that the principal axes of the SGS stress tensor be aligned with the resolved strain rate tensor. As Lund<sup>4</sup> has shown, although DSM accurately predicts the mean dissipation rate, it does not correlate with the channel flow DNS data of Kim *et al.*<sup>14</sup> as well as the Smagorinsky model in the local dissipation rate. A related and more serious problem arises when the dynamic model coefficient  $C$  is computed locally. Excessive energy backscatter occurs due to large fluctuations of the coefficient which leads to an exponentially growing instability.<sup>15</sup> These results show that DSM can accurately predict the mean flow quantities when the averaged model coefficient is used but gives inadequate representation of the local quantities.

It is reasonable to argue that the local noise in the DSM may be reduced by using a base model which does not assume the alignment of the SGS stress and the resolved strain rate tensors. A model of this nature is the scale similarity model proposed by Bardina *et al.*<sup>2</sup> It was found that the scale similarity model did not dissipate energy, however, when it was combined linearly with the Smagorinsky model, the resulting "mixed model" did dissipate energy and predicted turbulence statistics better than the Smagorinsky model alone. The mixed model, when coupled with the Gaussian filter, produced accurate results in LES of a turbulent channel flow,<sup>6</sup> and the scale-similarity term provided SGS backscatter in the near-wall buffer region.<sup>16</sup>

From another view point, the large fluctuations of the model coefficient  $C$  computed by DSM suggests that too much burden might have been put on  $C$ . The complete SGS dynamics is in  $\tau_{ij}$ , which is a tensor, while  $C$  is only a scalar function. As we will show in Sec. II,  $\tau_{ij}$  may be decomposed into two parts: a resolved part which is explicitly calculable and an uncalculable part. It may then be advantageous to calculate the former and only model the latter. We will show that the scale-similarity model of Bardina *et al.* and the resolved part of  $\tau_{ij}$  are closely related.

Based on the insights from the above, we propose to employ the mixed model as the base model in the dynamic closure. The new model, which one might call the dynamic mixed model, retains the favorable features of DSM and has several additional advantages. The scale similarity or the resolved term is expected to provide a major part of the SGS backscatter which will reduce the fluctuation of the model coefficient and enable the SGS model to have a better representation of the local flow dynamics.

In the following section we will describe the formulation of the dynamic mixed model. In Sec. III, we will present results from LES of lid-driven cavity flows which span the range from laminar through transitional to locally turbulent flows; data will be compared with previous experimental and computational results. Conclusions will be drawn in Sec. IV.

## II. MATHEMATICAL FORMULATION

For our computations, the governing equations are transformed into a general curvilinear coordinate system

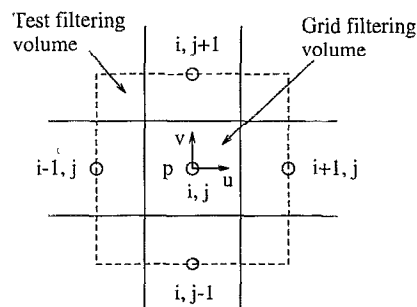


FIG. 1. Test filtering volume in two dimensions and the variable locations on a nonstaggered grid.

and discretized on a nonstaggered grid using a finite volume approach (Fig. 1). A fractional step method is employed and the pressure Poisson equation is solved with a multigrid method. Time marching is semi-implicit with the formal accuracy being second order in both space and time. The details of the numerical method and the test results of laminar flow cases can be found in Zang, Street, and Koseff.<sup>17</sup>

We now describe the formulation of the dynamic mixed model. For the incompressible and constant density flows considered here, the basic governing equations are the grid-filtered Navier-Stokes and continuity equations,

$$\frac{\partial \bar{u}_i}{\partial t} + \frac{\partial}{\partial x_j} (\bar{u}_i \bar{u}_j) = -\frac{\partial \bar{p}}{\partial x_i} + \nu \frac{\partial^2 \bar{u}_i}{\partial x_j \partial x_j} - \frac{\partial \tau_{ij}}{\partial x_j}, \quad (3)$$

$$\frac{\partial \bar{u}_j}{\partial x_j} = 0, \quad (4)$$

where the overbar denotes a grid-filtered variable. The effect of the unresolved subgrid scales is represented by the SGS stress

$$\tau_{ij} = \bar{u_i u_j} - \bar{u}_i \bar{u}_j. \quad (5)$$

Following Germano *et al.*,<sup>11</sup> we introduce a test-scale filter represented by a tilde. The purpose of doing this is to utilize the information between the grid- and test-scale filters to determine the characteristics of the SGS motion. By applying the test-scale filter to Eqs. (3) and (4), we obtain the sub-test-scale stress

$$T_{ij} = \widetilde{\bar{u_i u_j}} - \widetilde{\bar{u}_i} \widetilde{\bar{u}_j}. \quad (6)$$

Germano<sup>12</sup> showed that  $\tau_{ij}$  and  $T_{ij}$  are related by the following algebraic identity

$$\mathcal{L}_{ij} = T_{ij} - \tilde{\tau}_{ij}, \quad (7)$$

where the resolved stress  $\mathcal{L}_{ij}$  is

$$\mathcal{L}_{ij} = \widetilde{\bar{u_i u_j}} - \widetilde{\bar{u}_i} \widetilde{\bar{u}_j}. \quad (8)$$

We employ, as the base model, the mixed model of Bardina *et al.*<sup>2</sup> in which the constant has been adjusted by Speziale<sup>18</sup> from 1.1 to 1.0 to satisfy Galilean invariance. The anisotropic part of the SGS stress is then expressed as

$$\tau_{ij} - \frac{\delta_{ij}}{3} \tau_{kk} = -2C\bar{\Delta}^2 |\bar{S}| \bar{S}_{ij} + L_{ij}^m - \frac{\delta_{ij}}{3} L_{kk}^m, \quad (9)$$

where the grid-filter width is defined as

$$\bar{\Delta} = (\Delta x_1 \Delta x_2 \Delta x_3)^{1/3}. \quad (10)$$

Here,  $\Delta x_j$  ( $j=1,2,3$ ) is the grid spacing in the  $j$  direction,  $C$  is the model coefficient to be determined dynamically, and  $L_{ij}^m$  is

$$L_{ij}^m = \overline{u_i u_j} - \bar{u}_i \bar{u}_j. \quad (11)$$

The term  $L_{ij}^m$  can be expressed as

$$L_{ij}^m = \underbrace{\overline{u_i u_j} - \bar{u}_i \bar{u}_j}_{L_{ij}} + \underbrace{\overline{u_i' u_j'} - \bar{u}_i' \bar{u}_j'}_{\beta_{ij}}, \quad (12)$$

where  $L_{ij}$  is the Leonard stress resulting from the classical decomposition of the SGS stress<sup>19</sup> and  $\beta_{ij}$  is the Bardina scale-similarity term.<sup>2</sup> In the original mixed model,<sup>2</sup> the Leonard stress was computed explicitly while the cross term and the SGS Reynolds stress from the classical decomposition were modeled under the assumption that the SGS field could be approximated by the so-called “transfer field” which contains the larger eddies of the subgrid scales and also the smaller eddies of the resolved scales. The transfer field was represented by the difference between the filtered and the twice-filtered velocity fields,  $\bar{u}_i - \bar{\bar{u}}_i$ . It is easy to show that (9) is equivalent to the original formulation of the mixed model. It is worth noting here as well that alternative formulations of (9) are possible. Models such as those of Wong<sup>20</sup> (which is based on Speziale<sup>21</sup>) and Horiuti *et al.*,<sup>22</sup> which could preserve tensorial invariance and satisfy the realizability condition, might well be used in our general context to replace the Smagorinsky-style term. The approach and principles described here would, overall, be unchanged by such substitutions.

From Germano's redefinition of the stresses,<sup>23</sup> the term  $L_{ij}^m$  is the resolved part in the SGS stress. By decomposing the flow field as

$$u_i = \bar{u}_i + u_i' \quad (13)$$

and substituting into (5), we can express  $\tau_{ij}$  as

$$\begin{aligned} \tau_{ij} &= \overline{u_i u_j} - \bar{u}_i \bar{u}_j \\ &= \overline{(\bar{u}_i + u_i')(\bar{u}_j + u_j')} - \bar{u}_i \bar{u}_j \\ &= L_{ij}^m + C_{ij}^m + R_{ij}^m, \end{aligned} \quad (14)$$

where

$$\begin{aligned} L_{ij}^m &= \overline{u_i u_j} - \bar{u}_i \bar{u}_j \\ C_{ij}^m &= \overline{u_i' u_j'} + \overline{u_i' \bar{u}_j'} - (\bar{u}_i' \bar{u}_j' + \bar{u}_i' \bar{u}_j') \\ R_{ij}^m &= \overline{u_i' u_j'} - \bar{u}_i' \bar{u}_j' \end{aligned} \quad (15)$$

are referred to, respectively, as the “modified Leonard term,” the “modified cross term,” and the “modified SGS Reynolds stress.” These terms are expressed in the form of residuals and are invariant under Galilean transformation. The modified Leonard term is represented by resolved quantities while the other two terms make up the unresolved field. Germano's redefinition of stress shows that the mixed model essentially calculates the modified Leonard

term and only models the modified cross terms and the modified SGS Reynolds stress, i.e., the unresolved residual stresses.

The modified Leonard term for the test-scale filter,  $L_{ij}^T$ , is obtained by substituting (13) into  $T_{ij}$  [from (6)]

$$T_{ij} = \overline{\bar{u}_i \bar{u}_j} - \bar{\bar{u}}_i \bar{\bar{u}}_j \quad (16)$$

$$= \overline{(\bar{u}_i + u_i')(\bar{u}_j + u_j')} - \overline{(\bar{u}_i + u_i')(\bar{u}_j + u_j')} \quad (17)$$

$$= L_{ij}^T + C_{ij}^T + R_{ij}^T, \quad (18)$$

where

$$\begin{aligned} L_{ij}^T &= \overline{\bar{u}_i \bar{u}_j} - \bar{\bar{u}}_i \bar{\bar{u}}_j, \\ C_{ij}^T &= \overline{\bar{u}_i' u_j' + u_i' \bar{u}_j'} - (\bar{\bar{u}}_i' \bar{\bar{u}}_j' + \bar{u}_i' \bar{\bar{u}}_j'), \\ R_{ij}^T &= \overline{u_i' u_j'} - \bar{u}_i' \bar{u}_j'. \end{aligned} \quad (19)$$

Now assuming that the same mixed model can be applied to the test-scale filter, we have for the test-scale stress

$$T_{ij} - \frac{\delta_{ij}}{3} T_{kk} = -2C\bar{\Delta}^2 |\tilde{S}| \tilde{S}_{ij} + L_{ij}^T - \frac{\delta_{ij}}{3} L_{kk}^T, \quad (20)$$

where

$$\tilde{S}_{ij} = \frac{1}{2} \left( \frac{\partial \bar{u}_i}{\partial x_j} + \frac{\partial \bar{u}_j}{\partial x_i} \right), \quad |\tilde{S}| = (2\tilde{S}_{ij}\tilde{S}_{ij})^{1/2}, \quad (21)$$

and  $\bar{\Delta}$  is the test filter width which is larger than  $\bar{\Delta}$ . The expression for  $T_{ij}$  in (20) satisfies Galilean invariance.

By substituting (9) and (20) into (7), we have

$$\mathcal{L}_{ij} - \mathcal{H}_{ij} = -2C\bar{\Delta}^2 M_{ij} + \delta_{ij} P_{kk}, \quad (22)$$

where

$$\mathcal{H}_{ij} = \overline{\bar{u}_i \bar{u}_j} - \bar{\bar{u}}_i \bar{\bar{u}}_j, \quad (23)$$

$$M_{ij} = \alpha^2 |\tilde{S}| \tilde{S}_{ij} - |\tilde{S}| \tilde{S}_{ij}, \quad (24)$$

$$\alpha = \bar{\Delta}/\bar{\Delta}, \quad (25)$$

and  $P_{kk}$  is the isotropic term.

Using a least-square approach suggested by Lilly,<sup>24</sup> we have the expression for the model coefficient  $C$  from (22) as

$$C = - \frac{(\mathcal{L}_{ij} - \mathcal{H}_{ij}) M_{ij}}{2\bar{\Delta}^2 M_{ij} M_{ij}}. \quad (26)$$

The computed  $C$  is substituted into (2) and (9) to obtain the eddy viscosity and the SGS stress. In deriving the above equation, we have assumed that the variation of  $C$  is small in the test-filtering volume.

In the above model,  $\alpha$ , which is the ratio of the test scale to the grid scale, is the only input parameter. The SGS stress vanishes in laminar flows and at solid walls, exhibits correct asymptotic behavior in the near-wall region, and does not prohibit SGS backscatter. In addition to the favorable features of DSM, the dynamic mixed model (hereafter referred to as DMM) has several further advantages. First, DMM requires “less” modeling because of the explicit calculation of the modified Leonard term and the requirement to model only the residual stresses. Second,

the modified Leonard term,  $L_{ij}^m$ , can provide energy backscatter to the resolved scales. Comparing with DSM, we notice that by introducing the term  $L_{ij}^m$  in (9) the numerator of  $C$  has an extra term " $-\mathcal{H}_{ij}$ ." Because of the similarity between  $\mathcal{L}_{ij}$  and  $\mathcal{H}_{ij}$ , we expect that the magnitude of  $C$  will be smaller than that from DSM. As a result, DMM will reduce the excessive backscatter represented by  $C$  which causes the aforementioned numerical instability. Finally, the model does not require alignment of the principal axes of the SGS stress tensor  $\tau_{ij}$  and the resolved strain rate tensor  $\bar{S}_{ij}$ .

To discretize the grid-scale and the test-scale filters, we employ the box filter in physical space with the trapezoidal rule and linear interpolation (Appendix A). The length scale of the grid filter is equal to the grid size and the length scale of the test filter is twice of that (Fig. 1) resulting in an  $\alpha$  of 2. This value of  $\alpha$  was the optimal choice in the simulation of a turbulent channel flow.<sup>11</sup>

The box filter provides the necessary overlap between the resolved and the subgrid scales. When a sharp Fourier-space cutoff filter is used, however, the modified Leonard term,  $L_{ij}^m$ , represents only the SGS motion, and thus, has to be modeled. As a result, (9) reduces to (1). In addition, the modified Leonard term for the test-scale filter,  $L_{ij}^T$ , becomes identical to the resolved stress  $\mathcal{L}_{ij}$ . If  $L_{ij}^T$  is dropped from the right-hand side (rhs) of (20) based on the assumption that the models at the grid and the test scales are the same, then DMM reduces exactly to DSM. On the other hand, if  $L_{ij}^T$  is retained, it cancels out the resolved stress when the models are substituted into (7) and the result is that  $C$  vanishes. This difficulty arises because the sharp cutoff filter does not allow an overlap range between the resolved and the subgrid scales as do the Gaussian or box filters. One way to overcome it is to use two different cutoff filters to define the transfer field.<sup>25</sup> In a finite volume or finite difference method such as the present one, this difficulty does not appear because the box filter in physical space is usually employed.

In most of the previous work using the dynamic model, the flows under investigation have one or more homogeneous directions in which averaging could be employed.<sup>11,13</sup> For wall-bounded flows in complex geometries, there is usually no homogeneous direction. In the present work, after the model coefficient  $C$  is computed from (26), it is averaged locally in space within the test-filtering volume with a stencil of three grid points in each direction. The use of local averaging alone is, however, not enough to prevent solutions from blowing up because the eddy viscosity  $\nu_T$  computed from (2) using the locally averaged  $C$  could be negative and have a magnitude larger than the molecular viscosity  $\nu$ . The result is that the total viscosity or the total diffusivity is negative which, if this condition persists, will lead to an exponentially growing unstable solution. In order to guarantee that this does not happen, we set the total viscosity  $\nu + \nu_T$  to be zero whenever it becomes negative. However, for the cases computed in this work, the cutoff does not affect the flow significantly as the magnitude of the negative  $\nu_T$  is larger than  $\nu$  only at a very few grid points in a very localized region near the

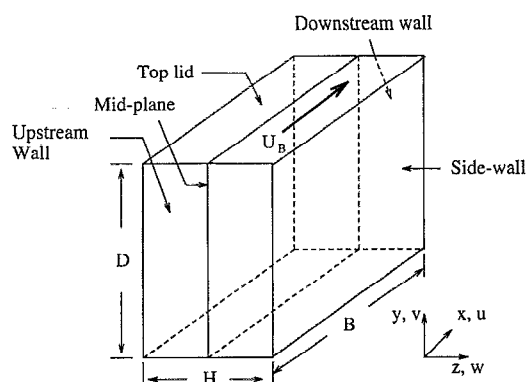


FIG. 2. Geometry and boundary condition of the lid-driven cavity flow.

upper right corner of the cavity. The use of DMM significantly reduces the number of grid points at which the cutoff is applied compared with DSM. Nevertheless, it remains desirable to have a more elegant way to prevent the numerical instability due to the occurrence of the negative total viscosity. A method based on the variational principle proposed by Ghosal *et al.*<sup>26</sup> or a model which represents SGS backscatter using a formulation other than an eddy viscosity (e.g., Leith<sup>27</sup>) are promising directions to explore.

### III. RESULTS AND DISCUSSION

We computed lid-driven flows in a three-dimensional cavity and compared the simulation results with the experimental data of Prasad and Koseff.<sup>28</sup> A schematic of the cavity together with the notations are given in Fig. 2. Three cases were considered with different Reynolds numbers and aspect ratios; the parameters and the grid resolution are given in Table I. The Reynolds number is based on the lid velocity  $U_B$  and the cavity length  $B$ . Past experiments<sup>28,29</sup> have shown that at Reynolds numbers lower than 5000, the flow is essentially laminar although inherent unsteadiness may occur. At Reynolds numbers higher than about 6000, flow becomes unstable near the downstream eddy. As the Reynolds number further increases, flow becomes increasingly turbulent near walls, and at Reynolds numbers higher than 10 000, the flow near the downstream eddy becomes fully turbulent. Therefore the three cases considered in the present work are in the laminar, transitional, and locally turbulent regimes, respectively.

The computational grid is nonuniform in the streamwise ( $x$ ) and vertical ( $y$ ) directions, but is spanwise uni-

TABLE I. Parameters of the cases run in the present study.

Case	$Re = U_B B / \nu$	Aspect ratios $B:D:H$	Grid points ( $x, y, z$ )	$\Delta x_{\min}/B$ , $\Delta y_{\min}/B$
1	3 200	1:1:1	(32,32,32)	$1 \times 10^{-2}$
2	7 500	1:1:0.5	(64,64,32)	$1 \times 10^{-2}$
3	10 000	1:1:0.5	(64,64,32)	$5 \times 10^{-3}$

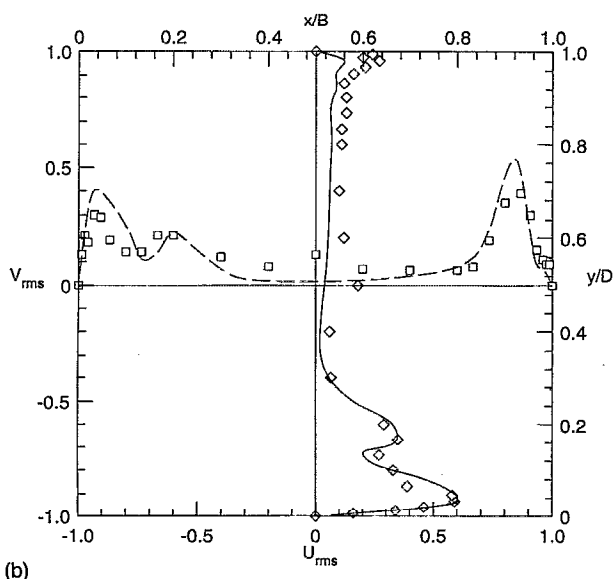
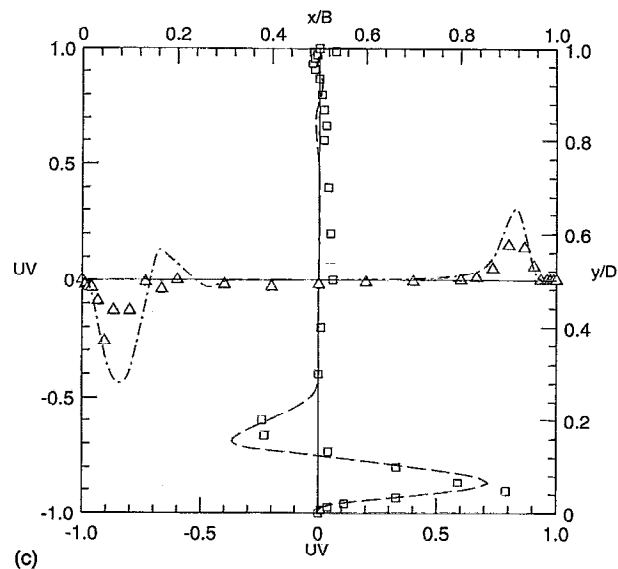
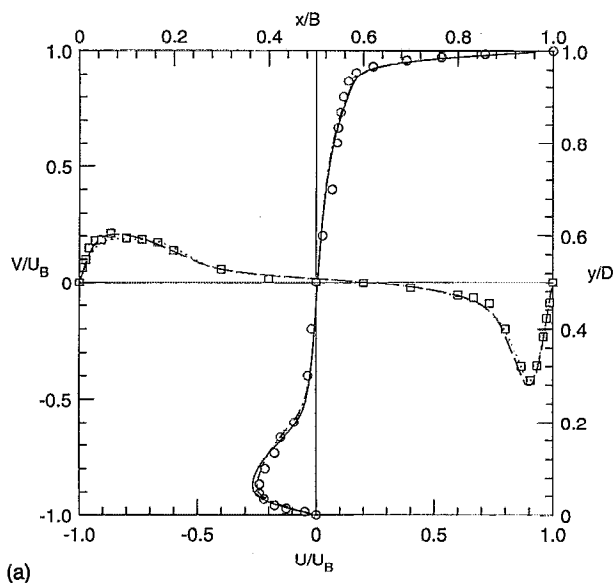


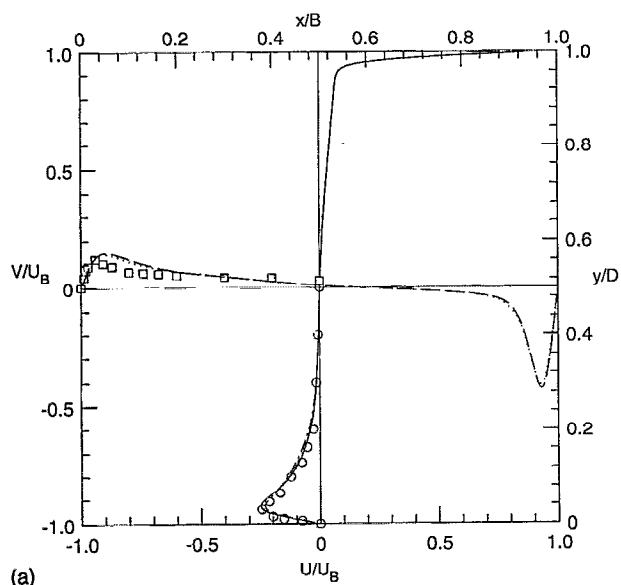
FIG. 3. Comparisons of quantities on the centerlines in the midplane with experimental data for case 1,  $Re=3200$ ,  $SAR=1.0$ . (a) Mean velocities,  $\circ$ :  $\langle u \rangle / U_B$ ,  $\square$ :  $\langle v \rangle / U_B$ , Prasad and Koseff (1989); — and ---: present with DMM; - - - and ····: Zang, Street and Koseff (1992a) with no model. (b) The rms velocities,  $\diamond$ :  $U_{rms} = 10\sqrt{\langle u''^2 \rangle} / U_B$ ,  $\square$ :  $V_{rms} = 10\sqrt{\langle v''^2 \rangle} / U_B$ , Prasad and Koseff (1989); — and ---: present with DMM. (c) The Reynolds stress,  $\square$ :  $UV = 500\langle u''v'' \rangle / U_B^2$ ,  $\triangle$ :  $500\langle u''v'' \rangle / U_B^2$ , Prasad and Koseff (1989); --- and - - - -: present with DMM.

form. Grid points are clustered near the walls in the  $x$  and  $y$  directions. The grid spacing is geometrically stretched away from the wall with the minimum value given in Table I. The initial condition is that the velocity field is at rest with no random perturbations. The computation was first carried out in a half of the cavity with half of the spanwise grid points. A symmetry boundary condition was specified at the midplane. After the flow was fully developed, the half flowfield was mirrored onto the whole cavity. Simulation then continued and statistics were collected after a relaxation time of about three advective time scale  $T$  of the cavity. The value of  $T$  was estimated as the time for a particle at the edge of the top boundary layer to travel back to its starting position in the cavity. The computed statistics were collected during periods of about  $5T$ . The experimental data from Prasad and Koseff<sup>28</sup> was averaged over 5 to  $10T$ .

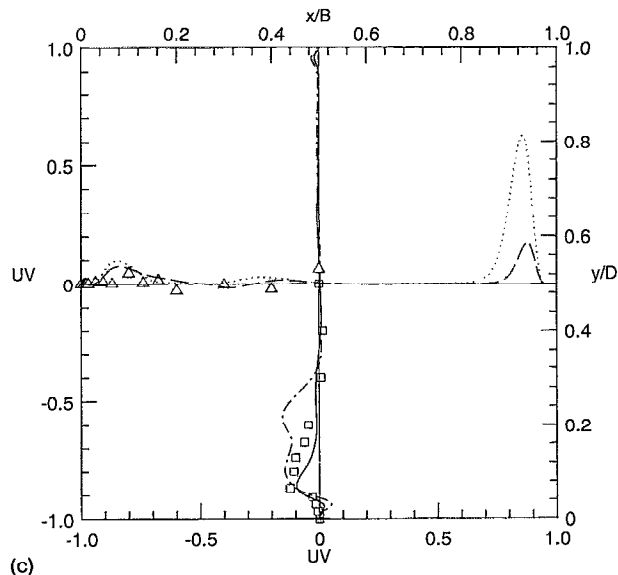
### A. Comparison with experiments

Figures 3(a), 3(b), and 3(c) show, respectively, the

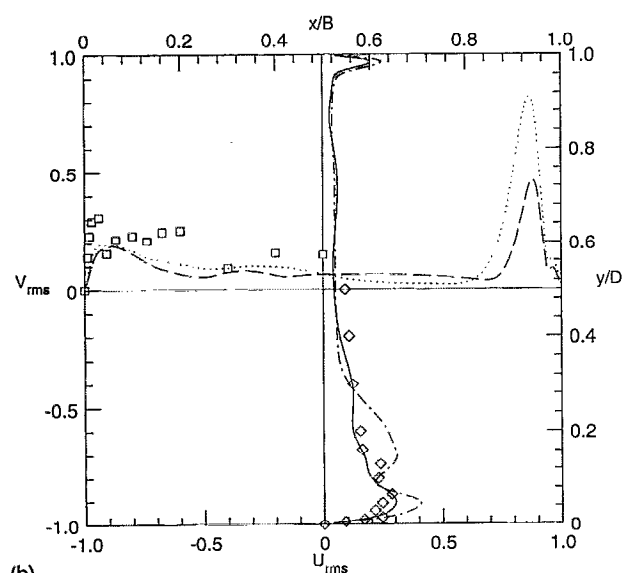
computed mean velocities  $\bar{u}/U_B$  and  $\bar{v}/U_B$ , the root-mean-square (rms) velocity  $\sqrt{\langle u''^2 \rangle} / U_B$  and  $\sqrt{\langle v''^2 \rangle} / U_B$  and the Reynolds stress  $\langle u''v'' \rangle / U_B^2$  on the center-lines in the mid-plane for case 1. Time averaging is denoted by  $\langle \cdot \rangle$  and  $u_i'' = u_i - \langle u_i \rangle$ . The spanwise aspect ratio  $SAR$  is defined as  $H/B$ . In 3(b) and 3(c), the rms and the Reynolds stresses are multiplied by a factor of 10 and 500, respectively for presentation purposes. Measurements by Prasad and Koseff<sup>28</sup> are given for comparison. It is noted that the Reynolds stress being discussed is from the conventional time averaging and should be distinguished from the SGS Reynolds stress  $\tau_{ij}$  defined in Eq. (5). In Fig. 3(a), profiles from Zang, Street, and Koseff,<sup>17</sup> which employed the same grid and did not use any SGS model, are also shown. Both the computed profiles agree extremely well with the experimental data. The fact that the two computed sets of data agree with each other shows that the effects of the SGS model diminish when the flow is essentially laminar as it is at this Reynolds number in the cavity. In Fig. 3(b), we see that the model accurately predicts the magnitude of the



(a)



(b)



(c)

FIG. 4. Comparisons of quantities on the centerlines in the midplane with experimental data for case 1,  $Re=7500$ ,  $SAR=0.5$ . (a) Mean velocities,  $\circ$ :  $\langle u \rangle / U_B$ ,  $\square$ :  $\langle v \rangle / U_B$ , Prasad and Koseff (1989); — and ---: present with DMM; - - - - and . . . . : Zang, Street and Koseff (1992b) with DSM. (b) The rms velocities,  $\diamond$ :  $U_{rms} = 10\sqrt{\langle u'^2 \rangle} / U_B$ ,  $\square$ :  $V_{rms} = 10\sqrt{\langle v'^2 \rangle} / U_B$ , Prasad and Koseff (1989); — and ---: present with DMM; - - - - and . . . . : Zang, Street, and Koseff (1992b) with DSM. (c) The Reynolds stress,  $\square$ :  $UV=500\langle u''v'' \rangle / U_B^2$ ,  $\triangle$ :  $500\langle u''v'' \rangle / U_B^2$ , Prasad and Koseff (1989); — and ---: present with DMM; - - - - and . . . . : Zang, Street, and Koseff (1992b) with DSM.

peaks of the rms velocity near the upstream, downstream, and the bottom walls while it underpredicts the peak near the top wall. The computation captures the two humps in the experimental profiles with remarkable accuracy. The Reynolds stress, shown in Fig. 3(c), is again very well represented by the simulation. While the calculation seems to overpredict the magnitude of the Reynolds stresses near the upstream and downstream walls, the overall agreement with the experimental data is excellent.

Figures 4(a)–4(c) display the same profiles for case 2 in which the Reynolds number is 7500. Besides the experimental data, profiles from Zang, Street, and Koseff<sup>30</sup> which were obtained using DSM on an identical computational grid are also shown for comparison. We can see that the mean velocities predicted by DSM and DMM in Fig. 4(a) are very close to each other. The computed profiles of  $u$  agree very well with the experimental data except that both calculations overpredict the thickness as well as the maximum velocity of the boundary layer on the upstream wall. The discrepancies between the computed and the

measured data near the upstream wall may originate from the small perturbations in the streamwise Taylor–Görtler-like (TGL) vortices<sup>29</sup> which grow in the free shear layer of the downstream eddy. These perturbations are propagated to the upstream wall through the interior where the grid is coarse; the insufficient resolution may contribute to the inaccuracy of the numerical solution near the upstream wall. The computed rms and the Reynolds stress, shown in Figs. 4(b) and 4(c), also agree well with experiments, except that the rms near the upstream wall is underpredicted. DMM gives a better agreement with the experiments than DSM in the profiles along the vertical centerline. In the boundary layer on the downstream wall, both the rms velocity and the Reynolds stress predicted by DMM are smaller than that by DSM. Although there is no experimental data for this case near the downstream wall, the results from DMM appear to be more consistent with the measurements by Prasad and Koseff at Reynolds numbers of 3200 and 10 000 with the same spanwise aspect ratios.

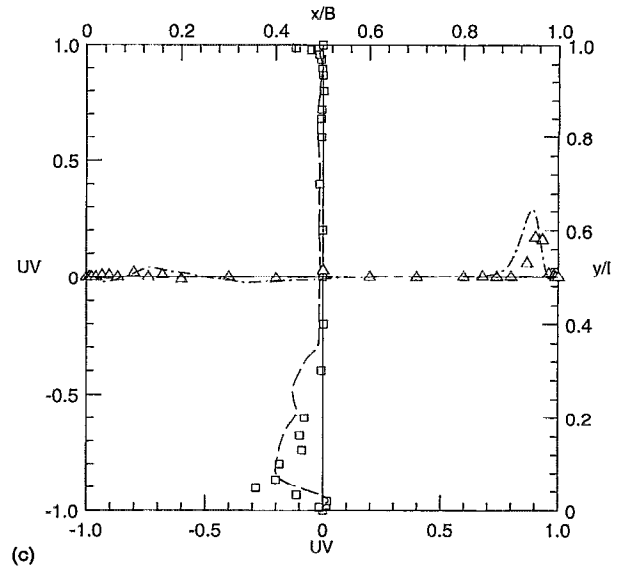
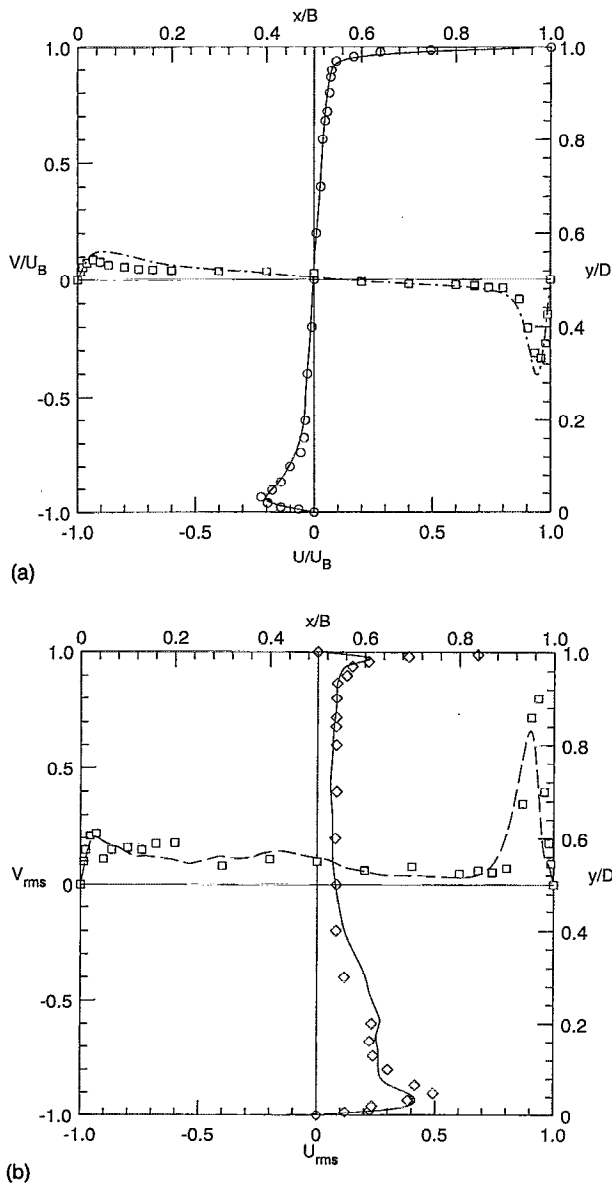


FIG. 5. Comparisons of quantities on the centerlines in the midplane with experimental data for case 1,  $Re=10\,000$ ,  $SAR=0.5$ . (a) Mean velocities,  $\circ$ :  $\langle u \rangle / U_B$ ,  $\square$ :  $\langle v \rangle / U_B$ , Prasad and Koseff (1989); — and ---: present with DMM. (b) The rms velocities,  $\diamond$ :  $U_{rms} = 10 \sqrt{\langle u'^2 \rangle} / U_B$ ,  $\square$ :  $V_{rms} = 10 \sqrt{\langle v'^2 \rangle} / U_B$ , Prasad and Koseff (1989); — and ---: present with DMM. (c) The Reynolds stress,  $\square$ :  $UV = 500 \langle u''v'' \rangle / U_B^2$ ,  $\triangle$ :  $500 \langle u''v'' \rangle / U_B^2$ , Prasad and Koseff (1989); --- and - - - -: present with DMM.

The same profiles for case 3 at Reynolds number of 10 000 are shown in Fig. 5. At this Reynolds number, the flow has become turbulent near the downstream eddy. A distinct inertial range was observed by Prasad and Koseff in their experiments. The computed centerline mean streamwise velocity profile agrees extremely well with the experiment. The computation slightly overpredicts the thickness and the maximum vertical velocity of the boundary layers on the upstream and downstream walls [Fig. 5(a)]. The centerline rms velocities also shows excellent agreement with the experiment although they are underpredicted near the top and the downstream walls [Fig. 5(b)]. In addition, the more difficult Reynolds stress is also predicted fairly accurately [Fig. 5(c)].

The number of grid points where the cutoff of negative eddy viscosity was executed was only a very small fraction of the total number of grid points. In the case where DSM is used,<sup>30</sup> the cutoff was executed at about 80 grid points at the stationary state, representing less than 0.1% out of a grid of  $64 \times 64 \times 32$  points. In case 3 where DMM is used,

this reduces to less than 0.01%, i.e., 8 grid points. In the laminar flow, case 1, no cutoff occurred as expected.

Overall, very consistent and favorable comparisons with the previous experimental and computational results were achieved. The discrepancies between the simulations and the experiments could be due to experimental uncertainty and the effect of numerical resolution. However, at the present time, collecting statistics on grids substantially finer than the ones presently used is prohibitively expensive.

## B. SGS effect on the Reynolds stress

The computed profiles in Figs. 3–5 are the large-scale quantities resolved by the grid, while the experimental data contains contributions from both the large scales and the small, subgrid scales. For example, the Reynolds stress measured in experiments is

$$e_{ij} = \langle u_i'' u_j'' \rangle \quad (27)$$



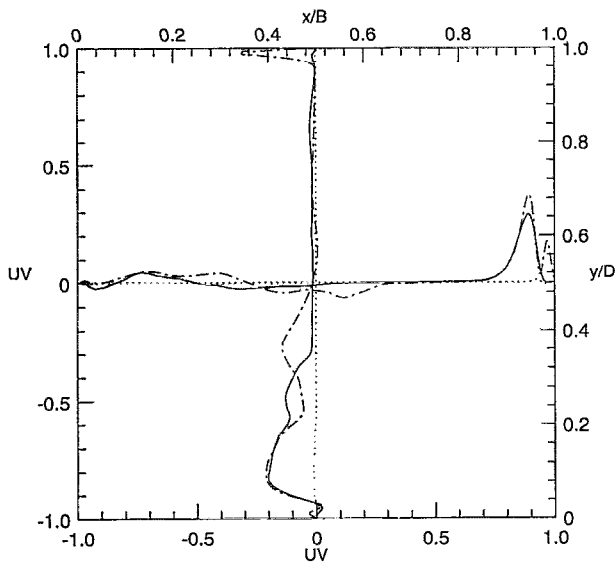


FIG. 6. The contribution from large and small, subgrid scales to the Reynolds stress on the centerlines in the midplane,  $Re=10\,000$ ,  $SAR=0.5$ . Symbols for  $UV$ ,  $\text{---}$ :  $500\langle \bar{u}''\bar{v}'' \rangle / U_b^2$ ,  $\cdots$ :  $5000\langle \epsilon_{ij} \rangle$ , from eddy viscosity part;  $\text{---}$ :  $5000\langle L_{ij}^m \rangle$ , from scale-similarity part.

while the computed Reynolds stress from the large eddy simulations is

$$c_{ij} = \langle \bar{u}_i'' \bar{u}_j'' \rangle. \quad (28)$$

It is desirable to establish a relation between  $e_{ij}$  and  $c_{ij}$  and obtain a measure of the contribution to the Reynolds stress from the subgrid scales besides that from the SGS model. If we assume that the spatial filtering and the time averaging operations commute, and that the long-time average of the SGS velocity is small and thus negligible, we obtain (see Appendix B)

$$\bar{e}_{ij} = \bar{c}_{ij} + \langle \tau_{ij} \rangle - \langle L_{ij} \rangle, \quad (29)$$

where  $\tau_{ij}$  is given in (5) and  $L_{ij}$  is the Leonard stress

$$L_{ij} = \bar{u}_i \bar{u}_j - \bar{u}_i \bar{u}_j. \quad (30)$$

The contribution of the subgrid scales to  $e_{ij}$  when  $i \neq j$  may be estimated by using the modeled  $\tau_{ij}$  in (9). In addition, the SGS contribution from the eddy-viscosity part  $\epsilon_{ij} = -2\nu_T \bar{S}_{ij}$  and the modified Leonard term  $L_{ij}^m$  in Eq. (9) may be estimated separately. In Fig. 6, we plot  $\langle \epsilon_{12} \rangle$  and  $\langle L_{12}^m \rangle$  on the centerlines in the midplane for case 3, together with the computed Reynolds stress  $c_{ij}$ . In the figure,  $c_{ij}$  is magnified by a factor of 500, while  $\langle \epsilon_{12} \rangle$  and  $\langle L_{12}^m \rangle$  are magnified by a factor of 5000. We can see that the SGS contribution from the eddy viscosity part  $\langle \epsilon_{12} \rangle$  is negligibly small; the contribution from the scale-similarity part  $\langle L_{12}^m \rangle$  is about an order of magnitude smaller than the large-scale Reynolds stress  $c_{ij}$  except in the vicinity of the top lid where the two quantities are of the same order. It is interesting to notice that profiles of  $\langle L_{12}^m \rangle$  and  $c_{12}$  are very similar to each other in the near-wall regions. The behavior of these quantities in cases 1 and 2 is similar. These results show that the time-averaged statistics are well represented by the large-scale quantities in the present calculations.

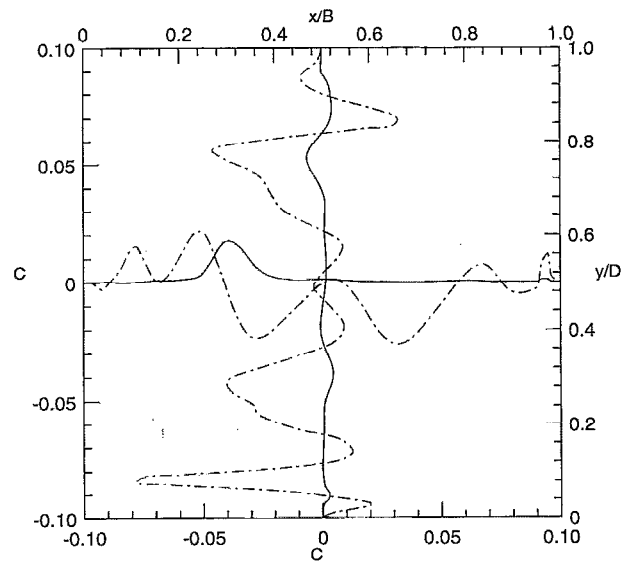


FIG. 7. The dynamically computed  $C$  on the centerlines in the midplane.  $\text{---}$ :  $C$  from DMM;  $\text{---}$ :  $C$  from DSM.  $Re=7500$ ,  $SAR=0.5$ .

### C. Model coefficient $C$

As discussed in Sec. II, we expect that, by employing the mixed model as the base model for the dynamic procedure, and in effect calculating the modified Leonard stress explicitly, the magnitude of the model coefficient  $C$  will be reduced compared with that from DSM. In Fig. 7, the values of  $C$  calculated using DMM and DSM are plotted along the centerlines in the midplane for case 2. We can see that the magnitude of  $C$  computed from DMM is indeed much smaller than that from DSM. Examining the values of  $C$  in the midplane, we find that for DSM,  $C$  ranges from  $-0.12$  to  $0.1$ , while for DMM,  $C$  ranges from  $-0.018$  to  $0.026$ .

In Fig. 8, contours of  $C$  in the midplane for case 3 are plotted. The bounds of  $C$  in this case are  $-0.03$  and  $0.04$  with an increment of  $0.005$ . We see that  $C$  is relatively large near the corner of the downstream and the bottom

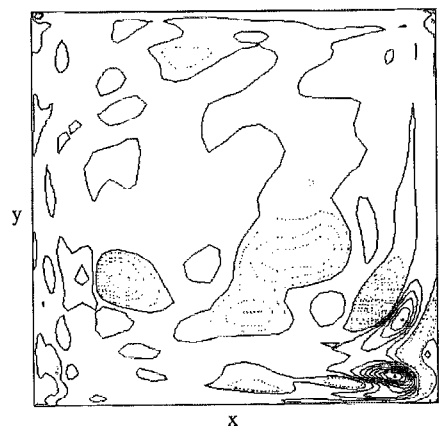


FIG. 8. The dynamically computed  $C$  in the midplane. Dotted lines represent negative values.  $Re=10\,000$ ,  $SAR=0.5$ .

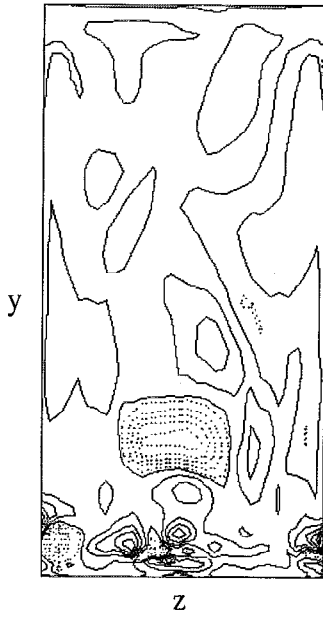


FIG. 9. The dynamically computed  $C$  in the spanwise-vertical ( $z$ - $y$ ) plane  $0.23B$  from the downstream wall ( $x/B=0.77$ ). Dotted lines represent negative values.  $Re=10\,000$ ,  $SAR=0.5$ .

walls. In Fig. 9, we plot  $C$  in a spanwise-vertical ( $z$ - $y$ ) plane  $0.23B$  from the downstream wall ( $x/B=0.77$ ). The bounds and the increment of  $C$  are the same as in Fig. 8. The value of  $C$  is large in the region near the bottom where streamwise vortices reside. Negative  $C$  appears in localized regions signaling SGS backscatter. As was shown previously by the present authors,<sup>30</sup> the ability of the present model to backscatter energy to large scales is important in sustaining the resolved-scale turbulent fluctuations in the simulation because the backscatter reduces the net SGS energy drain for the smallest of those resolved scales. In the regions where  $C$  is relatively large, its magnitude is of order 0.01 which is equal to the square of the commonly used value of the Smagorinsky constant. With the fact that a physical instability is known to occur near the downstream eddy, these results show that the SGS model is indeed capable of adjusting itself to local flow dynamics.

#### IV. CONCLUSIONS

The dynamic SGS eddy viscosity model has been modified by employing the mixed model as the base model. The new dynamic mixed model does not require alignment of the SGS stress tensor and the strain rate tensor. It is equivalent to explicitly calculating the modified Leonard stress and only modeling the rest of the terms in the SGS stress with the dynamic procedure. The model coefficient is computed locally together with a combination of a local spatial averaging and a cutoff. The new model should be coupled with a filter that allows overlap of the resolved and the subgrid scales. The box filter in physical space is used. If a Fourier sharp cutoff filter is used, either the dynamic

mixed model reduces to the dynamic SGS eddy viscosity model or two different filter levels should be used to define the transfer field.

The dynamic mixed model was incorporated into a finite-volume solution method. Large eddy simulations of lid-driven cavity flows in laminar, transitional, and turbulent regimes compare very favorably with past experiments and calculations. The data obtained using the new model shows better agreement with experiments than that using DSM. The magnitude of the dynamically computed model coefficient is significantly reduced compared with that from DSM. The contribution of the subgrid scales to the Reynolds stress is estimated. When compared with the large-scale quantities, this contribution is small in the present cases except that the modified Leonard term may be important near solid walls.

While more work still needs to be done to develop accurate, robust, and physically correct models for the large eddy simulation of complex turbulent flows, the present effort has provided interesting insights and successful simulations.

#### ACKNOWLEDGMENTS

The authors wish to thank Professors J. H. Ferziger and P. Moin and Dr. T. S. Lund for many helpful suggestions. The comments of the referees, particularly several relevant references, were useful and appreciated.

A Cray YMP computer time allocation was provided by the NCAR Scientific Computing Division. This research is supported by the National Science Foundation through Grant No. CTS-8719509 and by the Fluid Dynamics Program, Mechanics Division, Office of Naval Research through Grant No. N-00014-91-J-1200.

#### APPENDIX A: THE FORMULA FOR THE FILTERS

Figure 1 shows the filter volumes at the test and the grid scales. The test-scale filtered variable  $\bar{\phi}$  is computed with the trapezoidal rule,

$$\begin{aligned} \bar{\phi}_{i,j,k} = \frac{1}{8} & (\bar{\phi}_{i+1/2,j+1/2,k+1/2} + \bar{\phi}_{i-1/2,j+1/2,k+1/2} \\ & + \bar{\phi}_{i+1/2,j-1/2,k+1/2} + \bar{\phi}_{i-1/2,j-1/2,k+1/2} \\ & + \bar{\phi}_{i+1/2,j+1/2,k-1/2} + \bar{\phi}_{i-1/2,j+1/2,k-1/2} \\ & + \bar{\phi}_{i+1/2,j-1/2,k-1/2} + \bar{\phi}_{i-1/2,j-1/2,k-1/2}). \end{aligned}$$

Linear interpolation is employed to obtain a variable at locations where it is not defined. For example,  $\bar{\phi}_{i+1/2,j+1/2,k+1/2}$  is obtained by

$$\begin{aligned} \bar{\phi}_{i+1/2,j+1/2,k+1/2} = \frac{1}{8} & (\bar{\phi}_{i,j,k} + \bar{\phi}_{i+1,j,k} + \bar{\phi}_{i,j+1,k} \\ & + \bar{\phi}_{i+1,j+1,k} + \bar{\phi}_{i,j,k+1} \\ & + \bar{\phi}_{i+1,j,k+1} + \bar{\phi}_{i,j+1,k+1} \\ & + \bar{\phi}_{i+1,j+1,k+1}). \end{aligned}$$

For the grid-scale filter, the twice-filtered variable is

$$\begin{aligned}\bar{\phi}_{i,j,k} = & \frac{1}{8} (\bar{\phi}_{i+1/4,j+1/4,k+1/4} + \bar{\phi}_{i-1/4,j+1/4,k+1/4} \\ & + \bar{\phi}_{i+1/4,j-1/4,k+1/4} + \bar{\phi}_{i-1/4,j-1/4,k+1/4} \\ & + \bar{\phi}_{i+1/4,j+1/4,k-1/4} + \bar{\phi}_{i-1/4,j+1/4,k-1/4} \\ & + \bar{\phi}_{i+1/4,j-1/4,k-1/4} + \bar{\phi}_{i-1/4,j-1/4,k-1/4}).\end{aligned}$$

Similarly, for example,  $\bar{\phi}_{i+1/4,j+1/4,k+1/4}$  is obtained by linear interpolation, so that

$$\begin{aligned}\bar{\phi}_{i+1/4,j+1/4,k+1/4} = & \frac{1}{64} [27\bar{\phi}_{i,j,k} + 9(\bar{\phi}_{i+1,j,k} + \bar{\phi}_{i,j,k} \\ & + \bar{\phi}_{i,j,k+1}) + 3(\bar{\phi}_{i+1,j+1,k} \\ & + \bar{\phi}_{i+1,j,k+1} + \bar{\phi}_{i,j+1,k+1}) \\ & + \bar{\phi}_{i+1,j+1,k+1}].\end{aligned}$$

In the actual implementation, the following formulas are used to reduce the number of operations

$$\begin{aligned}\bar{\phi}_{i,j,k}^* &= \frac{1}{4} (\bar{\phi}_{i+1,j,k} + 2\bar{\phi}_{i,j,k} + \bar{\phi}_{i-1,j,k}), \\ \bar{\phi}_{i,j,k}^{**} &= \frac{1}{4} (\bar{\phi}_{i,j+1,k}^* + 2\bar{\phi}_{i,j,k}^* + \bar{\phi}_{i,j-1,k}^*), \\ \bar{\phi}_{i,j,k}^{\tilde{}} &= \frac{1}{4} (\bar{\phi}_{i,j,k+1}^{**} + 2\bar{\phi}_{i,j,k}^{**} + \bar{\phi}_{i,j,k-1}^{**}),\end{aligned}$$

and

$$\begin{aligned}\bar{\phi}_{i,j,k}^* &= \frac{1}{8} (\bar{\phi}_{i+1,j,k} + 6\bar{\phi}_{i,j,k} + \bar{\phi}_{i-1,j,k}), \\ \bar{\phi}_{i,j,k}^{**} &= \frac{1}{8} (\bar{\phi}_{i,j+1,k}^* + 6\bar{\phi}_{i,j,k}^* + \bar{\phi}_{i,j-1,k}^*), \\ \bar{\phi}_{i,j,k}^{\tilde{}} &= \frac{1}{8} (\bar{\phi}_{i,j,k+1}^{**} + 6\bar{\phi}_{i,j,k}^{**} + \bar{\phi}_{i,j,k-1}^{**}).\end{aligned}$$

## APPENDIX B: SGS CONTRIBUTION TO THE REYNOLDS STRESS

The experimentally measured Reynolds stress may be related to what is computed in a large eddy simulation in the following way. We first define the temporally fluctuating velocity as

$$u_k'' = u_k - \langle u_k \rangle, \quad (B1)$$

and the SGS velocity as

$$u_k' = u_k - \bar{u}_k. \quad (B2)$$

A spatially filtered variable is denoted by an overbar and time averaging is denoted by " $\langle \cdot \rangle$ ." The measured Reynolds stress  $e_{ij}$  and the computed stress  $c_{ij}$  are

$$e_{ij} = \langle u_i'' u_j'' \rangle, \quad (B3)$$

$$c_{ij} = \langle \bar{u}_i'' \bar{u}_j'' \rangle. \quad (B4)$$

Substitution of (B1) into (B3) leads to

$$e_{ij} = \langle u_i u_j \rangle - \langle u_i \rangle \langle u_j \rangle, \quad (B5)$$

since  $\langle u_i u_j \rangle = \langle u_i \rangle \langle u_j \rangle$ . Similarly, we have

$$c_{ij} = \langle \bar{u}_i \bar{u}_j \rangle - \langle \bar{u}_i \rangle \langle \bar{u}_j \rangle. \quad (B6)$$

By substituting (B2) into (B5), we obtain

$$e_{ij} = \langle (\bar{u}_i + u_i') (\bar{u}_j + u_j') \rangle - \langle \bar{u}_i + u_i' \rangle \langle \bar{u}_j + u_j' \rangle.$$

After rearranging, we have

$$e_{ij} = c_{ij} + \gamma_{ij}, \quad (B7)$$

where

$$\begin{aligned}\gamma_{ij} = & \langle \bar{u}_i u_j' \rangle + \langle u_i' \bar{u}_j \rangle + \langle u_i' u_j' \rangle - \langle \bar{u}_i \rangle \langle u_j' \rangle \\ & - \langle u_i' \rangle \langle \bar{u}_j \rangle - \langle u_i' \rangle \langle u_j' \rangle.\end{aligned} \quad (B8)$$

If we further assume that the long-time average of the SGS velocity is small, so that

$$\langle u_k' \rangle = 0, \quad (B9)$$

we can neglect the last three terms on the rhs of (B8) such that

$$\gamma_{ij} \approx \langle \bar{u}_i u_j' \rangle + \langle u_i' \bar{u}_j \rangle. \quad (B10)$$

We now seek to establish a relation between  $\gamma_{ij}$  and the SGS stress  $\tau_{ij}$ . The time average of  $\tau_{ij}$  is

$$\langle \tau_{ij} \rangle = \langle \bar{u}_i \bar{u}_j \rangle - \langle \bar{u}_i \bar{u}_j \rangle. \quad (B11)$$

Substituting (B2) into (B11), we have

$$\langle \tau_{ij} \rangle = \langle (\bar{u}_i + u_i') (\bar{u}_j + u_j') \rangle - \langle \bar{u}_i \bar{u}_j \rangle.$$

Assuming that spatial filtering operation and time averaging commute, we obtain, after rearrangements,

$$\langle \tau_{ij} \rangle = \langle \bar{u}_i \bar{u}_j - \bar{u}_i u_j' - u_i' \bar{u}_j + u_i' u_j' \rangle. \quad (B12)$$

Comparison between (B10) and (B12) leads to

$$\bar{\gamma}_{ij} \approx \langle \tau_{ij} \rangle - \langle L_{ij} \rangle, \quad (B13)$$

where  $L_{ij}$  is the Leonard stress given by

$$L_{ij} = \bar{u}_i \bar{u}_j - \bar{u}_i u_j'. \quad (B14)$$

Applying the filtering operation to (B7) and substituting (B13) into (B7), we have

$$\bar{e}_{ij} \approx \bar{c}_{ij} + \langle \tau_{ij} \rangle - \langle L_{ij} \rangle. \quad (B15)$$

Although the above equation only relates the spatially filtered values of  $e_{ij}$  and  $c_{ij}$ , it provides an approximate measure of the SGS contribution to the Reynolds stress. It is noted that the spatial average of the Leonard stress vanishes. Thus, in cases where there is a homogeneous direction, the average of (B15) in that direction would eliminate the effect of the Leonard stress.

<sup>1</sup>J. Smagorinsky, "General circulation experiments with the primitive equations. I. The basic experiment," *Mon. Weather Rev.* **91**, 99 (1963).

<sup>2</sup>J. Bardina, J. H. Ferziger, and W. C. Reynolds, "Improved turbulence models based on large eddy simulation of homogeneous, incompressible, turbulent flows," Ph.D. dissertation, Department of Mechanical Engineering, Stanford University, 1983.

<sup>3</sup>U. Piomelli, T. A. Zang, C. G. Speziale, and M. Y. Hussaini, "On the large-eddy simulation of transitional wall-bounded flows," *Phys. Fluids A* **2**, 2575 (1990).

<sup>4</sup>T. S. Lund, "On dynamic models for large eddy simulation," Annual Research Briefs, Center for Turbulence Research, Stanford University/NASA-Ames, 177 (1991).

<sup>5</sup>P. Moin and J. Kim, "Numerical investigation of turbulent channel flow," *J. Fluid Mech.* **118**, 341 (1982).

<sup>6</sup>U. Piomelli, P. Moin, and J. H. Ferziger, "Model consistency in large eddy simulation of turbulent channel flows," *Phys. Fluids* **31**, 1884 (1988).

- <sup>7</sup>V. Yakhot and S. A. Orszag, "Renormalization Group analysis of turbulence," *J. Sci. Comput.* **1**, 3 (1986).
- <sup>8</sup>A. Yakhot, S. A. Orszag, V. Yakhot, and M. Israeli, "Renormalization Group formulation of large-eddy simulations," *J. Sci. Comput.* **4**, 139 (1989).
- <sup>9</sup>K. Horiuti, "A proper velocity scale for modeling subgrid-scale eddy viscosities in large eddy simulation," *Phys. Fluids A* **5**, 146 (1993).
- <sup>10</sup>E. R. Van Driest, "On turbulent flow near a wall," *J. Aeronaut. Sci.* **23**, 1007 (1956).
- <sup>11</sup>M. Germano, U. Piomelli, P. Moin, and W. H. Cabot, "A dynamic subgrid-scale eddy viscosity model," *Phys. Fluids A* **3**, 1760 (1991).
- <sup>12</sup>M. Germano, "Turbulence: the filtering approach," *J. Fluid Mech.* **238**, 325 (1992).
- <sup>13</sup>P. Moin, K. Squires, W. Cabot, and S. Lee, "A dynamic subgrid-scale model for compressible turbulence and scalar transport," *Phys. Fluids A* **3**, 2746 (1991).
- <sup>14</sup>J. Kim, J. P. Moin, and R. Moser, "Turbulence statistics in fully developed channel flow at low Reynolds number," *J. Fluid Mech.* **177**, 133 (1987).
- <sup>15</sup>W. Cabot, "Large eddy simulation of passive and buoyant scalars with dynamic subgrid-scale models," *Annual Research Briefs, Center for Turbulence Research, Stanford University/NASA-Ames*, 191 (1991).
- <sup>16</sup>K. Horiuti, "The role of the Bardina model in large eddy simulation of turbulent channel flow," *Phys. Fluids A* **1**, 426 (1989).
- <sup>17</sup>Y. Zang, R. L. Street, and J. R. Koseff, "A non-staggered grid, fractional step method for time-dependent incompressible Navier-Stokes equations in general curvilinear coordinate systems," revised version submitted to *J. Comput. Phys.* (1993).
- <sup>18</sup>C. G. Speziale, "Galilean invariance of subgrid-scale stress models in the large-eddy simulation of turbulence," *J. Fluid Mech.* **156**, 55 (1985).
- <sup>19</sup>A. Leonard, "On the energy cascade in large-eddy simulations of turbulent fluid flows," *Adv. Geophys.* **18A**, 237 (1974).
- <sup>20</sup>V. C. Wong, "A proposed statistical-dynamic closure method for the linear or nonlinear subgrid-scale stresses," *Phys. Fluids A* **4**, 1080 (1992).
- <sup>21</sup>C. G. Speziale, "On nonlinear  $K-\epsilon$  and  $K-\epsilon$  models of turbulence," *J. Fluid Mech.* **178**, 459 (1987).
- <sup>22</sup>K. Horiuti, N. N. Mansour, and J. Kim, "A normal stress subgrid-scale eddy viscosity model in large eddy simulation," *Annual Research Briefs, Center for Turbulence Research, Stanford University/NASA-Ames*, 61 (1992).
- <sup>23</sup>M. Germano, "A proposal for a redefinition of the turbulent stresses in the filtered Navier-Stokes equations," *Phys. Fluids* **29**, 2323 (1986).
- <sup>24</sup>D. K. Lilly, "A proposed modification of the Germano subgrid scale closure method," *Phys. Fluids A* **4**, 633 (1992).
- <sup>25</sup>R. P. Garg, "Large-eddy simulation of detuned transition in plane channel flow," M.S. thesis, University of Maryland, College Park, MA, 1991.
- <sup>26</sup>S. Ghosal, T. S. Lund, and P. Moin, "A dynamic localization model for large-eddy simulation of turbulent flows," *Center for Turbulence Research Manuscript 139, Stanford University/NASA Ames Research Center* (1992).
- <sup>27</sup>C. E. Leith, "Stochastic backscatter in a subgrid-scale model: Plane shear mixing layer," *Phys. Fluids A* **2**, 297 (1990).
- <sup>28</sup>A. K. Prasad and J. R. Koseff, "Reynolds number and end-wall effects on a lid-driven cavity flow," *Phys. Fluids A* **1**, 208 (1989).
- <sup>29</sup>J. R. Koseff and R. L. Street, "Visualization studies of a shear driven three-dimensional recirculating flow," *J. Fluids Eng.* **106**, 21 (1984).
- <sup>30</sup>Y. Zang, R. L. Street, and J. R. Koseff, "Application of a dynamic subgrid-scale model to turbulent recirculating flows," *Annual Research Briefs, Center for Turbulence Research, Stanford University/NASA-Ames*, 85 (1992).